IN-33

p, 49

A NOVEL SILICON MICROMACHINED INTEGRATED MCM THERMAL MANAGEMENT SYSTEM

Progress report (year 2) and project renewal request for year 3 funding

to

NASA Lewis Research Center
Brookpark, Ohio

Performance period: March 1, 1998 to February 28, 1999

M.J. Kazmierczak, ███████
Department of Mechanical Industrial
and Nuclear Engineering
(513) 556-0259

H.T. Henderson, ███████
Department of Electrical and
Computer Engineering
(513) 556-4774

F.M. Gerner, ███████
Department of Mechanical, Industrial
and Nuclear Engineering
(513) 556-2646

TABLE OF CONTENTS

LIST OF FIGURES

LIST OF FIGURES (continued)

C. Additional Focus (Porous Wick)

While forced convection is a very effective method of cooling MCM's in terrestrial applications, it has a few drawbacks for space-based systems. The pump required to force the fluid through the heat exchanger adds weight to the system, and must also be electrically powered.

Loop heat pipes are passive devices, which do not require a pump. Also, since they take advantage of the latent energy of the working fluid, they are able to dissipate a very large heat flux. Unlike capillary pumped loops (CPL's) they do not have evaporator start-up problems. The following description of how a loop heat pipe can be utilized to cool high power density MCM's is taken from a proposal [4] written by the Center for Space Power at Texas A&M University (Best, 1997).
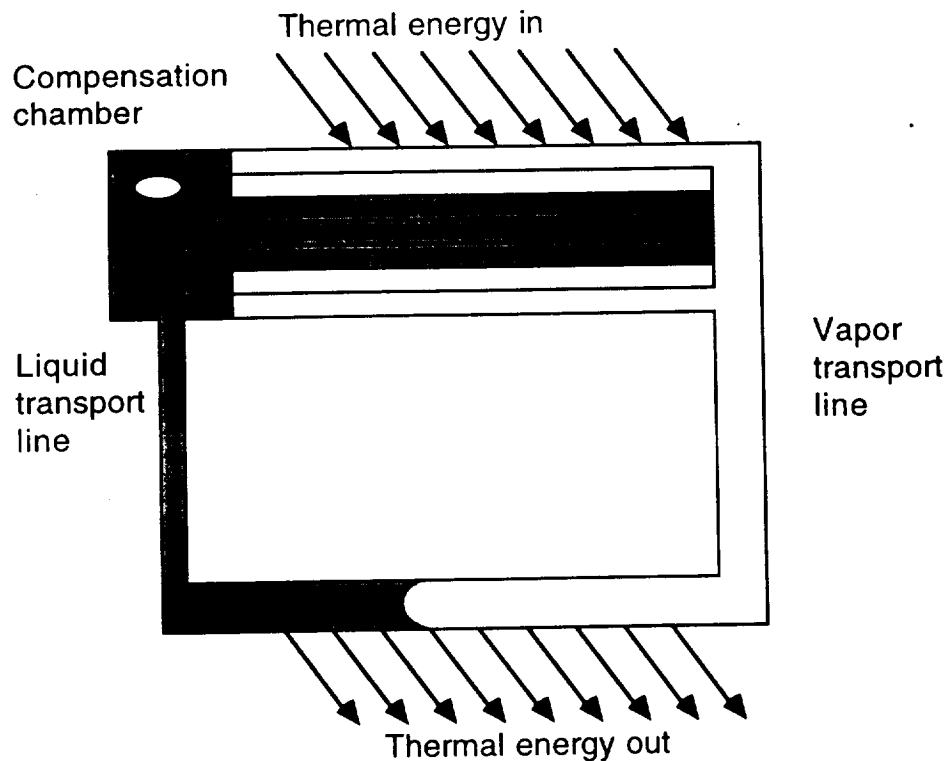
Fig. 4: Loop heat pipe schematic

"Figure (4) schematically shows a loop heat pipe composed of a compensation chamber, an evaporative structure, capillary transport loops, and a capillary condenser. Thermal energy from an MCM is transported to the evaporator wick by conduction and radiation. Evaporation from the wick produces vapor which travels through the vapor transport line to the condenser. The condenser transfers energy out of the working fluid

4

to a lower temperature external sink, converting the vapor to single phase liquid. The liquid returns to the evaporator through the liquid transport line which passes through the compensation chamber. The compensation chamber acts as an inventory controller for the system."

Currently one of the major limitations of a loop heat pipes ability to dissipate large heat fluxes is the porous wick. Conventional sintered particle wicks have a distribution of pore size and spacing which limit wick performance and hence maximum heat load for the loop heat pipe. Since the radii of curvature of the miniscus depends on pore size, the least favorable pore size determines the performance of the wick.

Several years ago it was found that under the proper conditions an HF-based electrolytic fluid will etch a porous "sponge-like" structure in silicon, where the walls, remain single crystalline silicon, as shown by x-ray analysis. The porosity will show an anisotropic directionality lying along the predominant current flow direction, perpendicular to the semiconductor surface. In recent years, several research groups have pursued the electroluminescense properties where the surface will continue to glow after being initially exposed to intense light. However, the controllability of the pore sizes, the porosity (volume occupied by etched-out open space) and the thermal properties are of interest in this work.

Also, etching activity can be lithographically patterned as with integrated circuits, and supplemental control can be had by adjusting the molarity of the etchant, the driving current, the local crystal doping (more activity in p+ regions) and even the intensity of directed light (as with a laser). Also, one can grow silicon dioxide on the surfaces of the pore walls under a high temperature oxide atmosphere (as we do in microelectronic frabrication), thus since oxide adds to the wall thickness we can fine-tune the pore size. Of course the oxide thermal properties are different (lower) than that of silicon, thus we can adjust the thermal properties after fabrication.

Micro-fabricating a porous wick in silicon allows one to create pores of uniform size and spacing. Also, it is possible to vary the diameter of individual pores across the thickness of the wick. This may greatly increase the maximum heat load for a layered heat pipe by preventing the miniscus from receding all of the way into the liquid. The goal of this part of our research is to create pores with diameter of order 1 micron and thereby greatly improve the thermal performance of loop heat pipes.

III. PAST YEAR IN REVIEW (Accomplishments)

B. Porous Wick Structure

1. Microfabrication of Porous Silicon: Background Information and Technique

In order to improve the performance of loop heat pipes it is necessary to fabricate a wick with a pore size of approximately 1 micron. Traditionally, porous silicon etching results in a sponge-like structure with pore sizes distributed from nanometers to hundreds of nanometers.

On the other hand, macro porous silicon can create arrays of straight and uniform holes through a flat silicon wafer. This type of porous structure is expected to yield better performance than the usual sponge-like ones. The uniform cylindrical shape also makes modeling and prediction much easier.

The fabrication process is electrochemical in nature. When properly biased, silicon etches in aqueous HF solution if electronic holes are present in the material. This is not the case for n-type silicon in the dark, where no etching takes place. Under light illumination however, electron/hole pairs are generated and etching then takes place. Thus, light intensity is a major parameter to be adjusted to control to the amount of silicon etched (see Figures 16-18). If the area of hole generation is limited to the backside of the wafer, the pores will grow straight toward it. This is achieved by including the IR blocking filter, limiting the depth of light penetration.

The etching takes place at a certain current density which is a function only of temperature and HF solution concentration. This means that if the latter is kept constant, the current density remains constant. Now, by changing the amount of light illumination the etching current does change. This can only mean that the effective area that is etched will change since the current density was constant. This area change in turn results in a change in pore diameter.

But there is a limit to how much the pore diameter can change. If a bare sample is etched, straight macropores are etched with their location across the wafer randomly distributed. Their diameter will center around a size which is determined by the doping concentration and their spacing will be determined by the illumination density. In practice, one must choose a certain doping concentration for the sample to achieve the desired pore diameter. Figure 21 shows branching because of too much doping for the desired pore size.

It is also possible to predetermine the pore pattern and thereby achieve a much more uniform distribution of pore diameters. This pore initiation step can be done by anisotropic etching. A photolithographic step defines an array of windows in a mask layer. Etched in, for example KOH, these result in an array of inverted pyramids. These pyramids are sufficient to initiate pore growth at those selected sites.

Thus, to achieve a desired pore pattern, one first chooses an adequate array of pore initiation sites. This will determine the pore pitch and array type (linear or staggered) of the porous sample. There are limits however in the photolithographic process and therefore pore spacing cannot be made arbitrarily small. Then, the actual pore diameter is set roughly by the chosen doping concentration of the silicon material and more precisely by the amount of light illumination. Since the etching current can be easily measured, the pore diameter can then be accurately controlled. Even slight changes in hole diameter are possible within the range allowed by the doping constraint. Pore depth is matter of time (parabolic function).

The etching process cannot be made to proceed through the total wafer thickness due to two reasons. First, the pores cannot grow towards the source of holes when they etch into the generation region; the field confinement of the tips is no longer effective. Pore branching is the result. Second, the HF etchant fluid would leak out of the setup and damage the optics. Instead of etching through the whole wafer, the solution employed here is to etch the pores through most (~ 90%) of the wafer thickness, and then etch the wafer from the backside until the pore region is exposed.

2. Etching System Setup

A new etching system was designed and built from scratch. (See Fig. 16 for system schematic and Figures 17 and 18 are actual photographs of the system.) We were able to use some knowledge and experience gained from our electrochemical etch stop rig, but the inclusion of a light source and other optical parts constituted a new challenge since HF as the etching solution does etch glass.

The rig was designed for operation in the upright position. This allows the resulting hydrogen gas to more easily detach from the wafer surface. All the parts in contact with the HF solution are made of Teflon or other compatible material. Since the illumination can lead to a temperature rise, a cooling loop was added (not shown), consisting of tubing, a peristaltic pump and a chiller.

The etching is controlled by a PC and HP Instruments system package (Fig. 18). A computer program was written which takes the etching parameters as the inputs and automatically controls the bias and current output. It also includes some safety shutdown features just in case the system experiences any abnormal operating conditions. Finally note that this system can etch the entire two-inch diameter wafers. This is essential for the eventual implementation of our thermal application into MEMS systems and is in contrast to the earlier pioneering work done on extremely small samples by the Munich group [8].
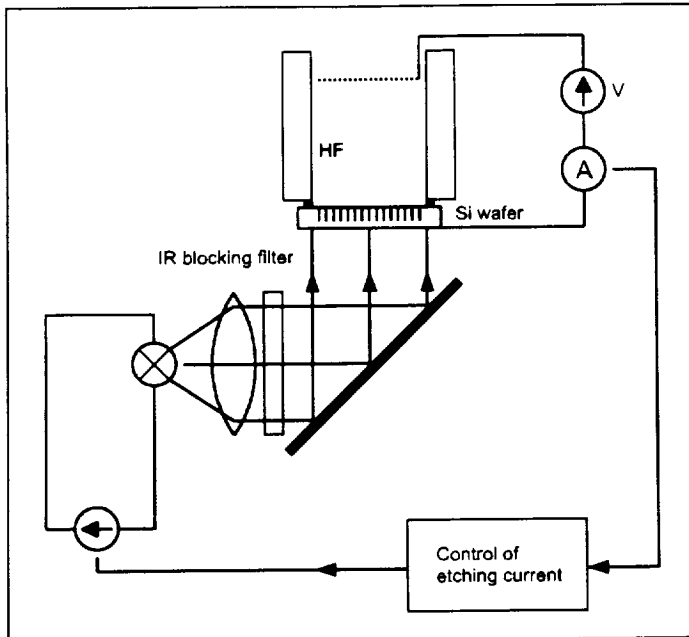
Fig. 16: Sketch of etch rig & control loop
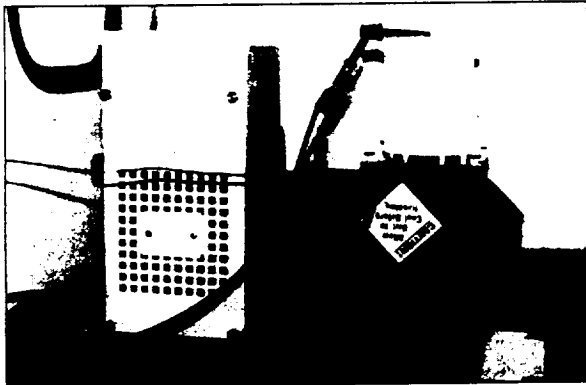
Fig. 17: Photograph of light source with etch rig
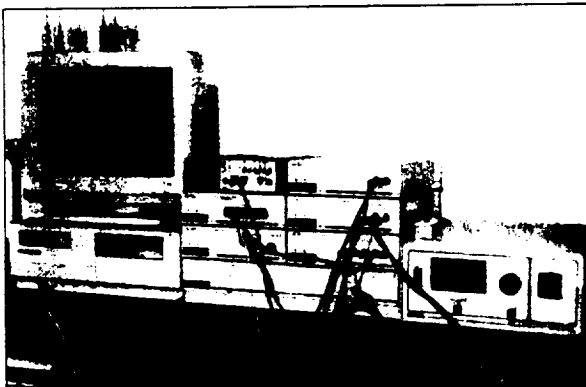
Fig. 18: Photograph of the PC and HP instruments

Microfabrication o Porous Structures: Preliminary Results and Success

a) Preliminary Samples: A couple of lessons had to be learned of course, before the desired pore geometry could be achieved

Fig. 19: Randomly distributed pores (no initiation) showed that the theory practically works. The etch depth was fairly predictable and the widening of the pores was induced by current-voltage curve experiments.
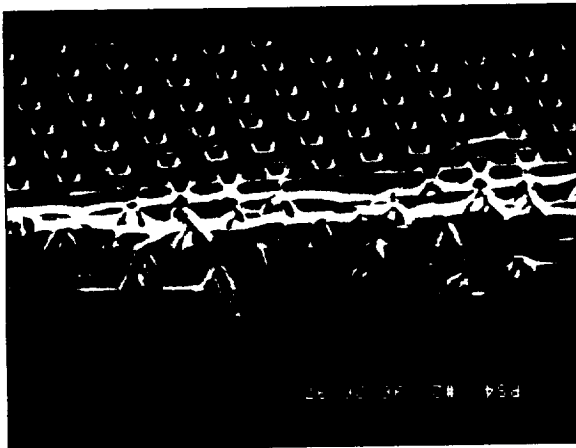
Fig. 20: Successful pore initiation using a mask; without IR blocking filter the pores tend to branch.

Fig. 21: Etched sample showing that too high of a doping concentration also leads to pore branching of a different kind,

b) Success with 5 micron holes and 20 micron pitch array
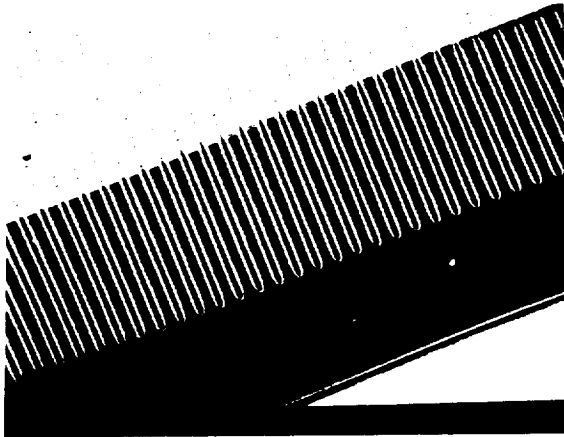
Fig. 22: First successful sample etched to a depth of 170 microns
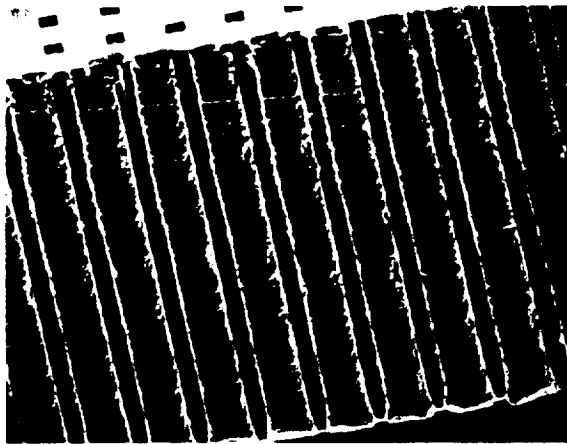
Fig. 23: The above sample after etching the remaining silicon from the backside.
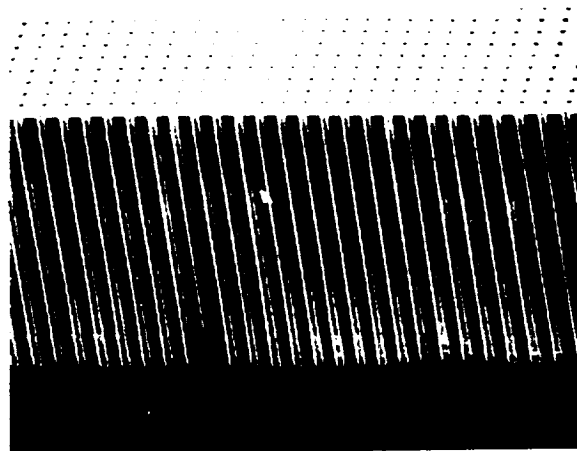
Fig. 24: Even deeper etching reveals some pore widening at these etching depths. This has not been reported previously and can be explained by HF depletion.

In closing this section we wish to acknowledge Dr. V. Lehmann [9] for his help and advice, an in particular, for his suggestions to include a uniform high doping step on the backside of the wafer. This small change was a major contribution to the success of the porous silicon experiments and resulted in excellent uniformity of the pore geometry across the wafer and considerable increase in the illumination efficiency.

26

4. Characterization of Porous Wick Properties

a) porosity and permeability: theoretical calculations

The **porosity** of a porous medium, ε, is simply defined as the fraction of the total volume of the porous matrix that is occupied by the open space [10]. Thus $1-\varepsilon$ is the fraction of the medium that is occupied by the solid region. The porosity of our given porous wick structure shown in Fig. 23 (consisting of 5 micron diameter circular through holes arranged in a square in-line pattern spaced 20 microns apart) is thus very easily calculated from the geometry and is $\varepsilon = 0.06$. Note that the porosity of the porous wick structure can be significantly increased by decreasing the spacing between the holes by using a different, smaller pitch, hole initiation mask.

The **permeability** K of the porous sample is a measure of the flow conductance of the fluid-flow through the fluid-saturated porous matrix, and is defined [10-12] according to Darcy's law by the following equation

$$u_D = \frac{K}{\mu}\left(-\frac{\partial P}{\partial x}\right) \tag{15}$$

where u_D represents the volume-averaged flow velocity within the porous matrix. Note that u_D should not be confused with the actual interstitial pore level velocity u, i.e. the local fluid velocity through the open spaces in the porous matrix, but rather u_D is the representative porous macroscopic *space*-averaged velocity through a "sufficiently large" volume of the porous matrix containing both the solid and open regions.

Thus, the permeability, K, can be thought of as the macroscopic manifestation [12] of highly viscous flow through the network of pores in the permeable structure, and as such its specific value depends on the resulting internal flow arrangement within that porous matrix. In general since the flow patterns created within most common types of porous medium are highly complex three-dimensional flows, the permeability constant appearing in Darcy's law is usually empirically derived in most situations.

However, for some very well-defined, simple, and repetitive porous structures of known geometry (such as the porous wick structure under investigation as shown in Fig. 23) the permeability can also be obtained from the application of the first principles of flow of viscous fluids at the pore level (i.e. viscous flow in tubes). Again, it should be emphasized that this approach is not feasible for very complex and irregular geometries, but only can be applied for very simple geometric structures. In short, it can be said that no single, overall general relationship exists between the pore structure and permeability; the few existing empirical, semiempirical, and first principle-based correlations all have to be used within the restrictions for which they have been developed.

Fortunately, for the case on hand, since the porous wick structure is composed of a well-defined small-scale network of straight channels, it is therefore possible to theoretically derive its permeability as a function of pore size and pore spacing from first principle using viscous flow theory. To this end the flow through each tube (i.e. pore level modeling) is modeled as laminar fully-developed Hagen-Poiseuille flow. (The laminar fully-developed assumption is reasonable due to the anticipated very small pore Reynold number, $Re_d \sim O[1]$, and due to the rather large L/D = 250/5 ratio.) Recalling from fluid mechanics [12], fully-developed laminar flow in a round tube of radius r_o is governed by

$$\frac{dP}{dx} = \mu\left(\frac{\partial^2 u}{\partial r^2} + \frac{1}{r}\frac{\partial u}{\partial r}\right)$$
(16)

Solving this equation subject to $u = 0$ at the cross-section periphery ($r = r_o$) yields

$$u = 2U\left[1 - \left(\frac{r}{r_0}\right)^2\right]$$

or
(17a,b)

$$U = \frac{r_0^2}{8\mu}\left(-\frac{\partial P}{\partial x}\right)$$

where u is the actual local fluid velocity, i.e. u(r), and U is the average or mean fluid velocity integrated across the channel (pore) cross-section.

Now considering once again the entire porous wick structure (global modeling) and assuming that Darcy law is applicable, which is a very valid assumption for slow flows in porous media, the flow when analyzed as passing through the porous medium as stated earlier is governed by the following equation

$$u_D = \frac{K}{\mu}\left(-\frac{\partial P}{\partial x}\right)$$
(18)

where u_D is the representative porous (volume-average) fluid velocity. In terms of the average fluid velocity in a single channel, U, and taking into account the pore density of the porous sample, let N/A be the number of pores per unit frontal area (tubes/m^2) and where A is the total (open and solid) frontal area (m^2), the porous fluid velocity can be expressed as

$$u_D = \frac{N\left(\pi r_0^2\right)}{A} U \qquad\qquad (19)$$

and which is simply equal to $u_D = \varepsilon U$ when one recalls the earlier definition of porosity.

Combining Equations (17b) - (19) one finds

$$\frac{N\left(\pi r_0^2\right)}{A} \frac{r_0^2}{8\mu}\left(-\frac{dP}{dx}\right) = \frac{K}{\mu}\left(-\frac{dP}{dx}\right) \qquad\qquad (20)$$

rearranging, permeability is then

$$K = \frac{\pi r_0^4}{8} \frac{N}{A} = \frac{r_0^2}{8}\varepsilon \qquad\qquad (21)$$

Equation (21) gives a relation between the permeability and the porosity for our given porous wick geometry based on the previous assumptions of fully-developed laminar flow and Darcy's law.

Figure 25 is a plot of the permeability as a function of the pore size for a given pitch pattern based on the above theory. As shown, the smaller the pitch, the higher the permeability of the porous wick for a given hole size. Smaller pitch means the holes are spaced closer together and thus there are a greater number of holes for fluid flow in a given cross-sectional area and thus less flow resistance. And, for a given fixed hole pitch pattern, we see that the permeability increases with hole size up to a maximum value limited by when the individual holes merge, i.e. the pore diameter equals hole pitch for this inline arrangement. Here, larger holes again mean more flow area (and higher porosity), therefore less flow resistance and thus higher permeability.

The dotted line in Fig. 25 is the empirical results taken from the latest U.S. and Russian research [13] in sintered power metal wick fabrication and is shown here for the sake of comparison. The plotted correlation is a curve fit of actual permeability measurements representing the "state-of-the-art" in porous wick fabrication using "advanced" fine pore processing technique. Although the theoretical permeability of our very first successfully micromachined porous sample (solid symbol, 5 micron dia. holes with 20 micron pitch; $K \sim 1.0E\text{-}14$ m^2) is slightly less in magnitude than the best that is currently available, this figure clearly reveals the great potential to easily exceed the current limitations by simply micromachining smaller size holes packed closer together.
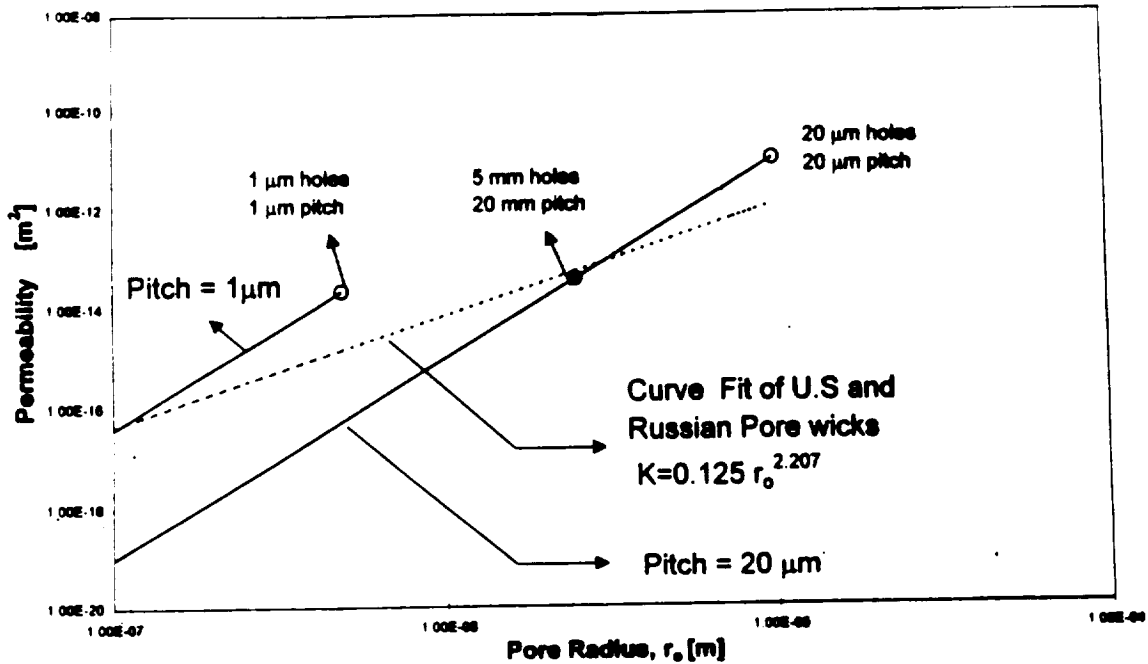
Figure 25 - Theoretical permeability of the micromachined porous wick structure as a function of the selected pore radius and pitch with comparison to current state-of-the-art wick technology

b) porosity and permeability: experimental testing

Porosity of the porous sample are to be determined two ways. First, the porosity of the porous sample can be easily calculated from its definition given the exact geometry of the holes. The representative pore size and pore hole distribution measurements are obtained from close up photographs taken under the microscope of the porous sample at discrete locations. Circular holes and a repetitive pattern is assumed to extend throughout the entire porous specimen and any nonuniformity in the individual pore hole or in the pore distribution pattern will result in some inaccuracy in the porosity calculation. However, judging from the excellent pore uniformity obtained in the successfully fabricated porous sample (Fig. 23) we feel that the slight deviations in shape will cause a relatively small error in the porosity calculation. Second, it is also possible to the determine the porosity of the porous sample by weight analysis by using a very sensitive

mass scale if the overall dimensions of the porous sample are known. The advantage of this method is that the exact <u>internal</u> pore structure does not have to be measured to use this technique. However, the uncertainty in the weight measurement and the uncertainty in the overall sample's dimensions are the major source of errors to consider when measuring porosity using this second methodology.

The sample <u>permeability</u> can be determined if the fluid flow through the wick and the resulting pressure drop across the wick are known, recall Darcy's law, Equation (15). These quantities are to be experimentally measured using our fluid flow testing loop facility shown below in Figure 26. Note that this flow circuit is essentially the same water testing loop facility used in the previous microchannel cooling experiments [5] i.e. the same pump, instrumentation, etc., but has been slightly reconfigured with a new test section (see insert) specifically designed to securely hold the porous sample in line with the water flow. The pressure drop and fluid flow rate are to be measured electronically using a pressure transducer and turbine flow meter, respectively, and the data recorded using the PC and data acquisition system. We have just successfully completed "leak testing" the new test section and are now ready to begin permeability testing of the porous samples. (See section IV.B.2 for further details.)
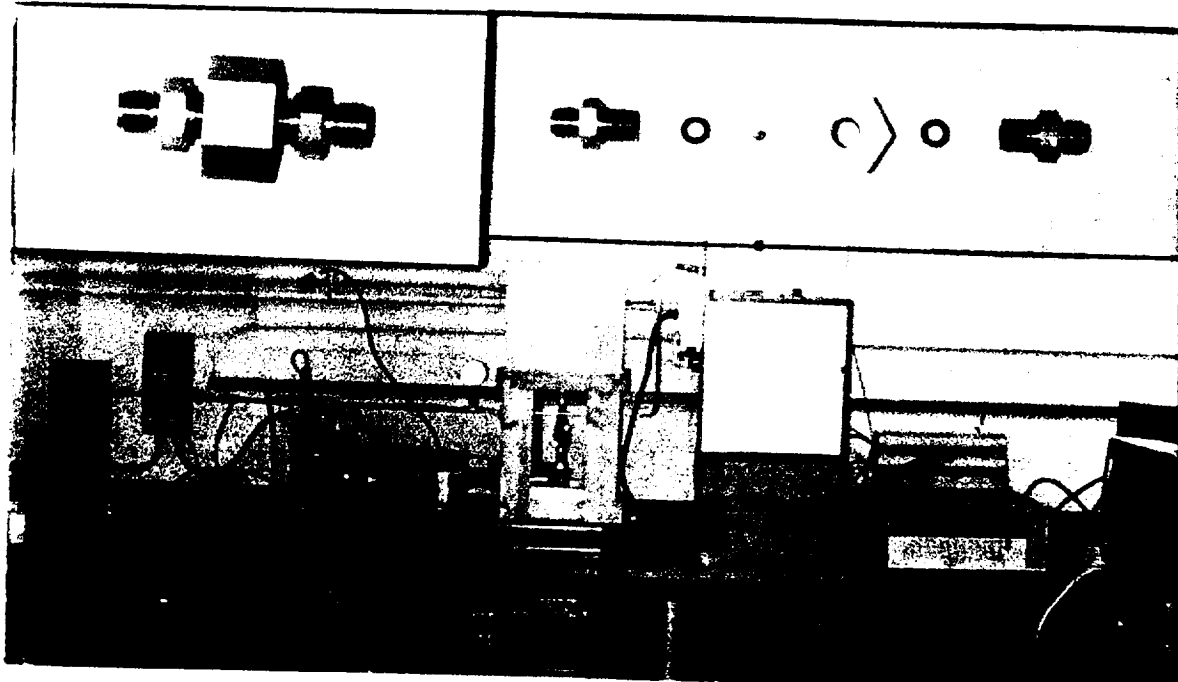
Figure 26 - Porous wick permeability testing loop; insert shows close-up of test section

c) effective thermal conductivity of porous silicon wick

The thermal performance of the wick is paramount to the successful operation of the loop heat pipe, and therefore it's thermal conductivity no doubt will be an important factor. In anticipation of this fact we have theoretically estimated, as best we can, the thermal conductivity of our porous silicon wick structures by borrowing freely from the results of the latest thermal conductivity studies found in the porous media literature [10-12, 14-16].

In general we know [10] that the thermal conductivity of a porous medium depends on many variables. Functionally,

$$k_{eff} = f(k_s, k_f, \varepsilon, \text{microstructure, other considerations}) \tag{22}$$

where

k_{eff} - effective thermal conductivity of saturated porous medium
k_s - thermal conductivity of solid phase
k_f - thermal conductivity of fluid phase
ε - porosity

Clearly we are taking a <u>macroscopic</u> point of view (i.e. considering <u>volumetrically averaged</u> or global quantity, not pore level or local value of thermal conductivity) in dealing with k_{eff}. (In treating the wick structure as a porous media the solid phase is silicon and the open pore region is the fluid region, liquid or vapor.)

There are two extremely simple 1-D models which establish the upper and lower bounds for k_{eff} of a porous medium (in general) and are based upon <u>assuming</u> either a pure *parallel* type connections (Eq. 23) or a pure *series* type connections (Eq. 24) of the constituents making up the porous medium. Basically this amounts to assuming the porous material is a 1-D <u>heterogeneous</u> material of known structure.

Temperature T_1

ks	k_f

Temperature T_2

(Parallel)

$$k_{eff} = (1-\varepsilon)k_s + \varepsilon k_f \tag{23}$$

Temperature T_1

k_s
k_f

Temperature T_2
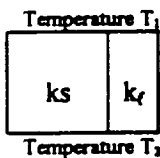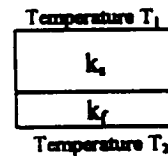
(Series)

$$\frac{1}{k_{eff}} = \frac{(1-\varepsilon)}{k_s} + \frac{\varepsilon}{k_f} \tag{24}$$

Often, however, porous material is composed of packed beds of particles and as such contains a combination of both types of heat transfer paths (series and parallel). Empirically this arrangement has been shown to behave according to

$$k_{eff} = k_s^{(1-\epsilon)} k_f^{\epsilon} \qquad \text{(geometric mean)} \qquad (25)$$

as long as k_f is not two much different than k_s , with the value of $k_{eff,geometric}$ falling somewhere in between the two limits just described. Also note that regularly or randomly packed beds to a very good approximation can be treated as a homogeneous medium with respect to the effective thermal conductivity, i.e. no directional dependence.

More accurate formulas for k_{eff} are available in the literature but become increasingly more complex, requires additional information, and are more "system specific" applicable to a particular type of porous medium. For example, better correlations exists (based on 2-D and 3-D models) specific for a given particle geometry (spheres, rods, etc.) with known packing arrangements (simple cubic, body center cubic, etc.). Also, if packing is random but tend to take on a certain distribution, let's say four different kinds of packing structures, a range of k_{eff} can be theoretically predicted based on the probability distribution of finding those certain types of packing structures within the porous medium. Equations (26)-(27) listed below is of this last type and gives the upper and lower bounds for the traverse conductivity $k_{eff,traverse}$ for a two-dimensional anisotropic fibrous material composed of needle-shaped fibers, all being arranged in parallel with each other, in a gaseous or solid matrix of different thermal conductivity [14].

$$\frac{k_{eff}}{\sqrt{k_s k_f}} \le \left[\frac{1+\delta_v(\beta-1)}{\sqrt{\beta}} \left\{ 1 - \frac{\{\delta_s(1-\delta_v)(\beta-1)^2\}}{2[1+\delta_v(\beta-1)][1+(\beta-1)\delta_v + 2(\beta-1)(1-2\delta_v)G]} \right\} \right] \qquad \textbf{(Upper limit)} \qquad (26)$$

$$\frac{k_{eff}}{\sqrt{k_s k_f}} \ge \sqrt{\beta} \left[\beta - \delta_v(\beta-1) - \left\{ \frac{\{\delta_s(1-\delta_v)(\beta-1)^2\}}{2(1-\beta)\delta_v + 2\beta + 4(\beta-1)(2\delta_v-1)G} \right\} \right]^{-1} \qquad \textbf{(Lower limit)} \qquad (27)$$

Where

$$\delta_v = 1-\epsilon \qquad\qquad \beta = \frac{k_s}{k_f} \qquad\qquad G=0.25 \text{ for Circle shaped cells}$$

Note that the recommended effective thermal conductivity (according to reference [14]) in the axial direction (parallel to the fibers) for the same anisotropic fibrous porous medium structure is simply given by the earlier Eq (23) Hence, to summarize, for this stated fibrous arrangement it's concluded [14] that the very simple parallel 1-D model is reasonable for predicting $k_{eff,axial}$ but the $k_{eff,traverse}$ values range somewhere between the upper and lower 2-D limits as given by Eqs (26) and (27), respectively (which are significantly larger in magnitude than the 1-D series model estimate of Eq. (24) due to multi-dimensional heat conduction in the medium)

These different thermal conductivity models just described are used to estimate the effective thermal conductivity of our porous silicon wick structure, saturated with <u>water</u> in Table 1, and saturated with <u>water-vapor</u> in Table 2, for select values of porosity. The results of the wick saturated with water is also shown plotted in Figure 27. Inspection of Tables 1-2 along with Figure 27 reveals the following:

i) The value of k_{eff} of the wick structure saturated with water or saturated with water-vapor is approximately the same for $k_{eff,axial}$ (Eq. 23), $k_{eff,traverse\ upper\ limit}$ (Eq. 26), and $k_{eff,geometric\ mean}$ (Eq. 25) models, i.e. compare the values of Table 1 and Table 2, but differ significantly for $k_{eff,traverse\ lower\ limit}$ (Eq. 27) and $k_{eff,series}$ (Eq. 24) models.

2) $k_{eff,axial}$ (Eq. 23) varies linearly with porosity (thus is a strong function of ε).

3) $k_{eff,traverse}$ 2-D upper and lower limits, Eqs.(26) - (27) $>>$ $k_{eff,1-D\ series}$, Eq. (24). (Hence the 1-D series model greatly underestimate the value of $k_{eff,traverse}$). Also note that $k_{eff,traverse}$ dependence on porosity diminishes as ε increases, now dominated by the value of the low conductivity fluid).

4) $k_{eff,geometric\ mean}$, Eq. (25), is <u>always within</u> the upper and lower bounds of $k_{eff,traverse}$ and is a much simpler equation to use to calculate the effective thermal conductivity.

5) $k_{eff,axial} > k_{eff,traverse\ 2-D\ upper\ limit}$ for all values of porosity.

In applying the above results to the wick geometry there are two additional facts that one should keep in mind:

6) The wick geometry is <u>not</u> exactly the same as that of the 2-D fibrous insulation system modeled and analyzed in ref. [14]; however both systems are reasonably similar in shape to one another to a certain degree, note also that ref. [14] geometry is the closest that can be found to the wick structure in the literature without doing a more extensive search.

7) The results of reference [14] is based solely on a <u>theoretical study</u> only and was <u>not</u> validated experimentally at the time (although latter reference to this study imply that the reported results are reasonable.)

Hence, given these last two comments imply that one should use <u>caution</u> in applying the results of Eq. (23) and Eqs.(26)-(27) (or Eqs. (23) and (25)) to determine $k_{eff,axial}$ and $k_{eff,traverse}$, respectively, of the porous silicon wick. The results obtained using the above equations therefore should be viewed only as <u>rough estimates only, not actual values</u> of the effective thermal conductivity of the porous wick structure. Finite element modeling [16] are recommended (and/or actual thermal conductivity testing of the wick is suggested) if more precise values of thermal conductivities of the wick structure are needed. (However we do feel that the equations listed above reveal the proper trends, i.e. effect of porosity, thermal conductivity of the saturating fluid (water vs. water-vapor) directional dependence (axial vs. traverse), etc, and, in fact, can provide reasonable first cut estimates.)

Table 1 $K_s = 128$ W/m °C $K_f = 0.648$ W/m °C (Silicon / Water)

Porosity	Eq. 23	Eq. 24	Eq.25	Eq. 26	Eq. 27
0.2	102.530	3.176	44.472	82.359	13.946
0.5	64.314	1.289	9.107	32.807	2.528
0.7	38.840	0.924	3.164	12.379	1.309
0.9	13.360	0.720	1.099	2.037	0.798

Table 2 $K_s = 128$ W/m °C $K_f = 24.6 \times 10^{-3}$ W/m °C (Silicon / Water-Vapor)

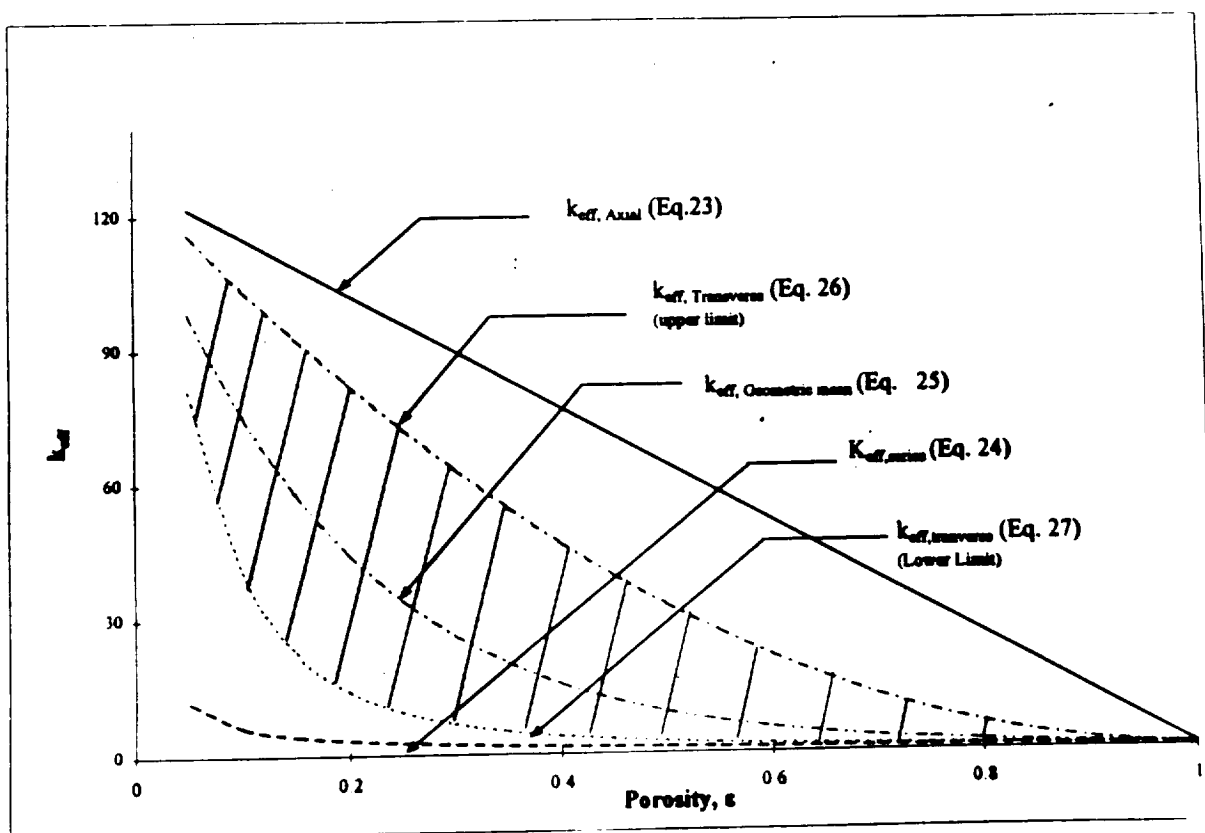| Porosity	Eq. 23	Eq. 24	Eq. 25	Eq. 26	Eq. 27
0.2	102.405	0.123	23.118	81.937	0.611
0.5	64.012	0.049	1.774	32.031	0.098
0.7	38.417	0.035	0.320	11.553	0.050
0.9	12.822	0.027	0.058	1.309	0.030

Fig. 27 Thermal conductivity (theoretical) of the micromachined silicon porous wick structure saturated with water as a function of porosity

B. Porous Wick Structure

1. Microfabrication of Porous Silicon Wick Structures

Our goal next year is to fabricate a second set of porous silicon test specimens, again with straight through holes, but this time the pores fabricated in the silicon wafer will be smaller and spaced much closer together. In particular, additional pore initiation masks will be fabricated which allow for pore arrays with a 4-micron pitch. This is at the lower limit of our photolithography equipment. Both linear and staggered pore arrays will be made and the pore diameter will be reduced to about 1 micron in these samples.

The slight widening of the pores as observed in our earlier results (Fig. 24) will also be investigated and studied. We will control this behavior in our earlier 5-micron diameter pores samples by adjusting the light intensity. Then, if necessary, it will also be dealt with accordingly in the latter samples containing the smaller hole arrangements. Since this effect has not been previously reported in the literature our findings may result in a short publication.

The fabrication of a porous silicon wafer with the much finer pore patterns will essentially conclude the macro porous silicon fabrication efforts here at UC, although it needs to be stated that much more work still remains to be done before a micromachined silicon porous wick can be successfully integrated into a loop heat pipe. (See section B.3 for further discussion.)

2. Testing of Porous Silicon Samples

The porosity and permeability of the porous silicon samples with be measured here at UC using the techniques and test set-up as described in section III.B. 4.b. Testing of the 5 micron pore sample is currently in progress; the smaller pore samples will also be similarly tested when available. It is our hope that the measured permeability will closely follow the theory but any major deviation in the data from theory will be resolved. Thermacore and Texas A&M are expected to confirm our results by doing repetitive testing on similar samples (fabricated by UC) using their own testing facilities. The effective thermal conductivity of the samples will not be measured.

3. Microfabrication of Advanced Porous Structures

As mentioned in the Project Description section, there may be some advantage to varying the pore diameter across the thickness of the wick. This should allow one to operate under normal conditions with one radius of curvature, and utilize another radius of curvature to prevent the meniscus from receding into the liquid. Also, by shortening the length of the smaller diameter section, the hydrostatic pressure drop can be reduced.

Several discussions have occurred between the University of Cincinnati, NASA Lewis, DTX and Texas A&M. Two or three concepts have been proposed. Before any final design, however, DTX and Texas A&M will have to perform some detailed calculations to specify the actual dimensions which are desired. The University of Cincinnati can then determine if it is possible to fabricate. Of course several iterations may be necessary before a workable design can be reached.

V. CLOSING

Although many multi-chip module (MCM) approaches have been tried or used in recent years, the one herein proposed is quite revolutionary, but yet realistic. Work is progressing at a steady rate on schedule and major achievements have already been realized at this point in time. Ultimately, the micromachined integrated MCM thermal management system should demonstrate that the chip temperatures can be maintained at the present levels while increasing the volume density by as much as two orders of magnitude at the chip level. The resulting savings in mass and volume we feel will prove to be extremely beneficial to NASA.

Also, an additional endeavor that is to be accomplished during the course of this project is to use MEMS technology to fabricate "porous" silicon, with specific "micromachined" geometric characteristics, to form the ultimate in wick structures for use in heat loops. To the best of our knowledge porous silicon has never before been considered for such a thermal application but has rather been investigated for its luminescent properties (not fully understood). However, since the porosity, anisotropy and pattern configuration can be controlled it could revolutionize the area of semiconductor cooling, thermosyphon evaporation, etc. Moreover, the planar technology is a batch-processing technique, which will ultimately be very inexpensive.

Of course successful creation of porous silicon wicks will be of great benefit for utilizing this MCM concept in space applications. Eliminating the pump will further reduce the mass and volume of the complete thermal management system.

Thus, we feel that this project embodies several rather revolutionary and potentially very pragmatic areas of thermal development by cross-fertilization of several disciplinary areas heretofore overlooked.

VI. BIBLIOGRAPHY

1a. Doty, J., 1996, " Fabrication of Flow Sensor Device," *Ph.D. Dissertation*, University of Cincinnati, Cincinnati, Ohio.

1b. Narayan, B., 1996, "Modeling of a Microflow Sensor," *M.S. Thesis*, University of Cincinnati, Cincinnati, Ohio.

2. Ramadas, P., 1997, "Micro Heat Pipes Fabrication and Testing," *Ph.D. Dissertation*, University of Cincinnati, Cincinnati, Ohio.

3. Badran, B., 1997, "Micro Heat Pipes: Design, Analysis and Testing," *Ph.D. Dissertation*, University of Cincinnati, Cincinnati, Ohio.

4. Best, F., 1997, "Cooling of Multi-Chip Modules by Loop Heat Pipes with Optimize Pore Structures," Proposal submitted to NASA Lewis Research Center from the Center for Space Power, Texas A&M University, College Station, Texas.

5. Harms, T., 1997, "Heat Transfer and Fluid Flow in Deep Rectangular Liquid-Cooled Microchannels Etched in a (110) Silicon Substrate," *M.S. Thesis*, University of Cincinnati, Cincinnati, Ohio.

6. Madhusudana, C.V., 1996, *Thermal Contact Conductance*, Springer-Verlag, New York, NY.

7a. Yovanovich, M.M., 1981, "New Contact and Gap Conductance Correlations for Conforming Rough Surfaces," *AIAA Paper* 81K - 1164, pp. 1-6.

7b. Antonetti, V.W., 1992, "Statistical Variability of Thermal Interface Conductance," *NSF/DITAC Workshop*, Melbourne, Australia, pp. 37-45.

7c. Kennard, E.H., 1958, *Kinetic Theory of Gases*, McGraw-Hill, New York, NY, pp. 311-327.

8. Lehmann and Gruning, 1997, "The Limits of Macropore Array Fabrication," *Thin Solid Films*, pp. 13 - 17.

9. Lehmann and Gruning, 1997, *private communications.*

10. Kaviany, M., 1995, *Principles of Heat Transfer in Porous Media*, Springer-Verlag, New York, NY, 2nd Ed.

11. Nield, D. and Bejan, A., 1992, *Convection in Porous Media*, Springer-Verlag, New York, NY.

12. Bejan, A., 1984, *Convection Heat Transfer*, John Wiley & Sons, New York, NY.

13. Gernert, N., Baldassarre, G., and Gottschlich, J., 1996, "Fine Pore Loop Heat Pipe Wick Structure Development," *Proceeding of Aerospace Atlantic Conference*, SAE paper # 961319, pp 1-10.

14. Tien, C. and Vafai, K., 1979, "Statistical Bounds for the Effective Thermal Conductivity of Microspheres and Fibrous Insulation," *Prog. Astronaut. Aeronaut.* 65, 135-148.

15. Nield, D.A., 1991, "Estimation of the Stagnant Thermal Conductivity of Saturated Porous Media," *Int. J. Heat Mass Transfer*, Vol. 34, No.6, pp.1575-1576.

16. Bakker, K., 1997. "Using the finite element method to compute the influence of complex porosity and inclusion structures on the thermal and electrical conductivity," *Int. J. Heat Mass Transfer*, Vol. 40, No.15, pp.3503-3511.

APPENDIX B

A Novel Silicon Micromachined Integrated

MCM Thermal Management System

H. T. Henderson, J. Pilchowski, A. Hölke

University of Cincinnati

Center for Microelectronic Sensors and MEMS

Dept. of Elect. and Comp. Engr. and Comp. Sc.

M. Kazmierzak, F. M. Gerner, A. Saleh,

X. Liu, E. Peters, R. Reynolds

University of Cincinnati

Dept. of Mech., Ind. and Nucl. Engr.

Agenda

1. **MCM - Thermal Management System**

    * **Microfabrication**

        board etching, chip separation, sensors, etc.

    * **Thermal Analysis**

        contact resistance, 3-D thermal model
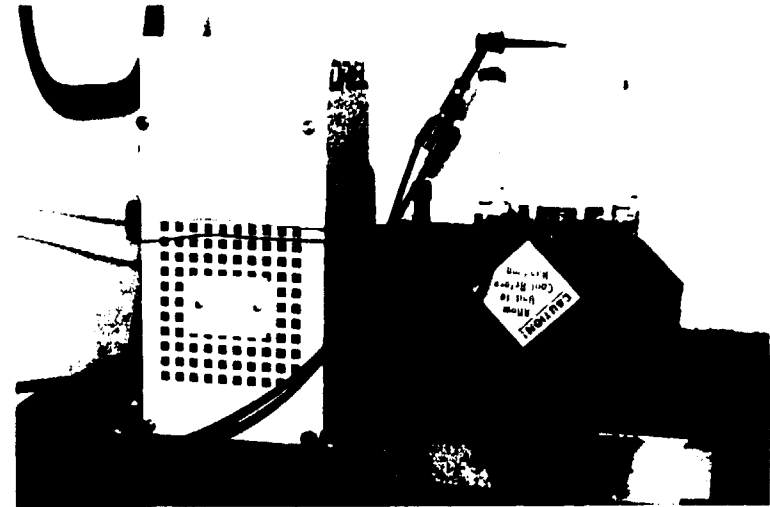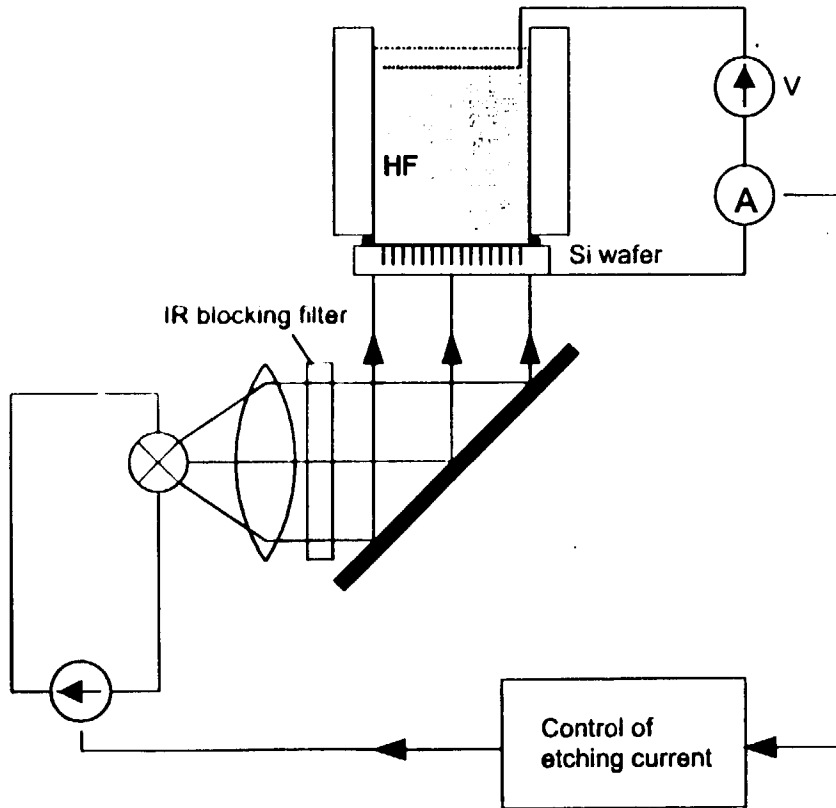
2. **Porous Wick Structure**

    * **Microfabrication**

    * **Permeability Testing**
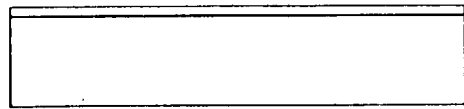
Porous Wick Structure

- ❏ microfabrication facility
- ❏ Ø 5µm × 20µm pitch fabrication
- ❏ new results
- ❏ permeability testing

Etch Rig

Fabrication Sequence

1.-2. Oxidation, BOE on Backside

SiO$_2$

n - Si

3. N$^+$ - Diffusion

SiO$_2$

n - Si

n$^+$ - Si

4. Metal Deposition
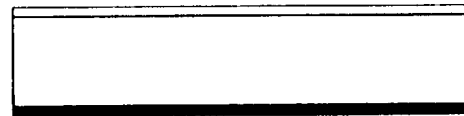
SiO$_2$

n - Si

n$^+$ - Si

Al

5. Metal Lithography and Etching
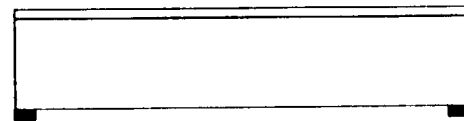
6. Pore Initiation Lithography
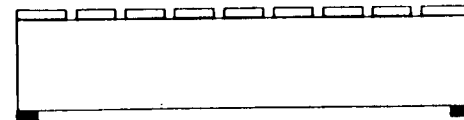
7. Pore Initiation Etching (KOH)
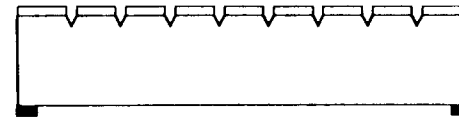
8. Porous Silicon Etching (HF)

9., 10. Al Etching, Reoxidation

11., 12. Backside BOE, Wafer Thinning (TMAH)

13. BOE
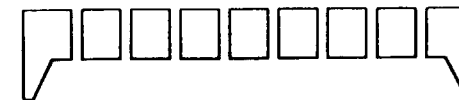
Ø 5μm × 20μm pitch fabrication
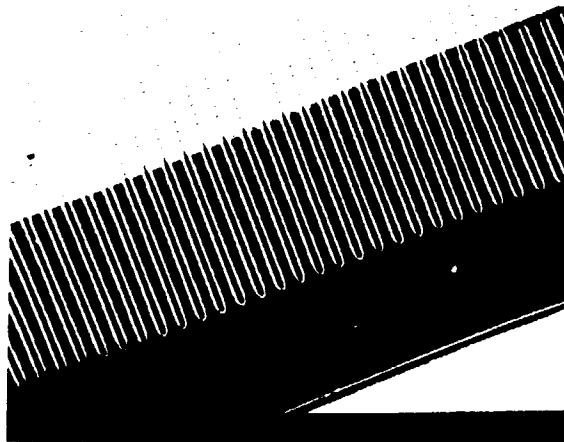
First successful sample etched to a depth of 170 microns
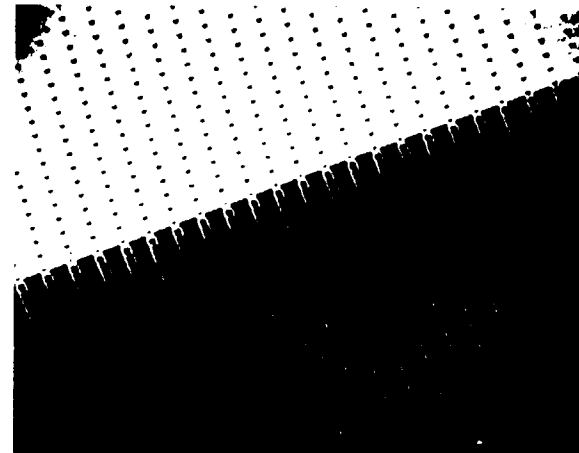
Deeper etching (260 μm) reveals some pore widening.
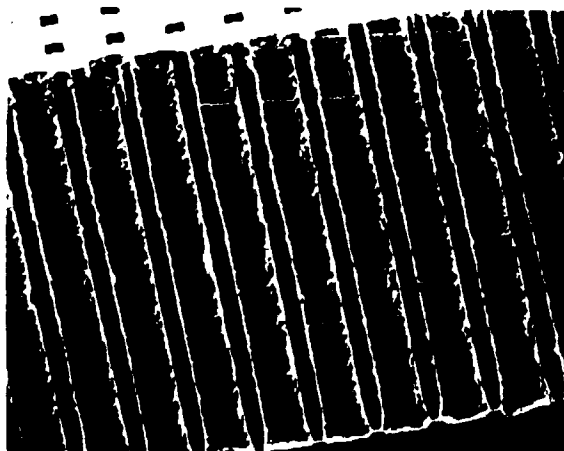
The above sample after etching the remaining silicon from the backside
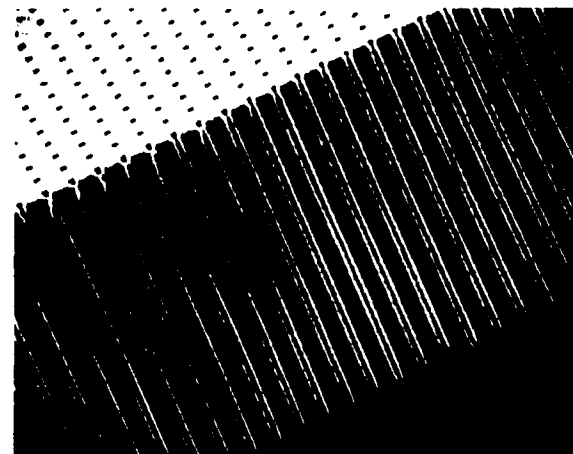
Deep etching with adjusted etching current yields straight pores

New Results

❑ **Ø 1-3μm × 4μm pitch fabrication**

❑ **new mask, parameters**

Ø 2.5μm × 4μm pitch
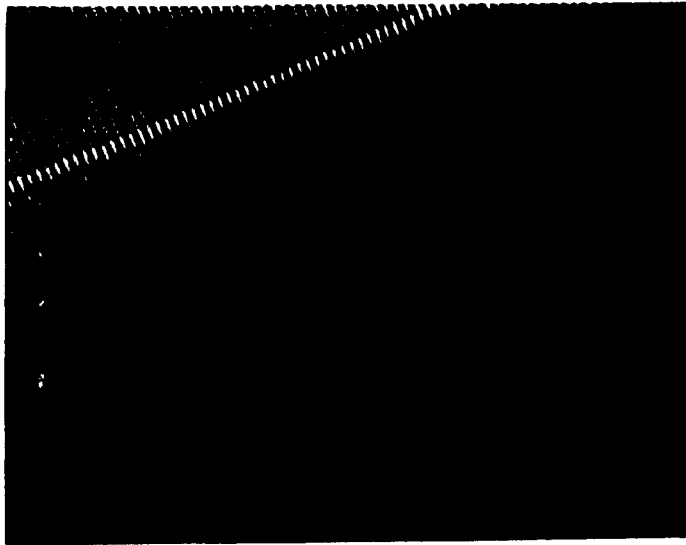
Ø 1.1μm × 4μm pitch

Permeability Testing

manometer

column hight

sample

reservoir

pump

0.5 µm filter
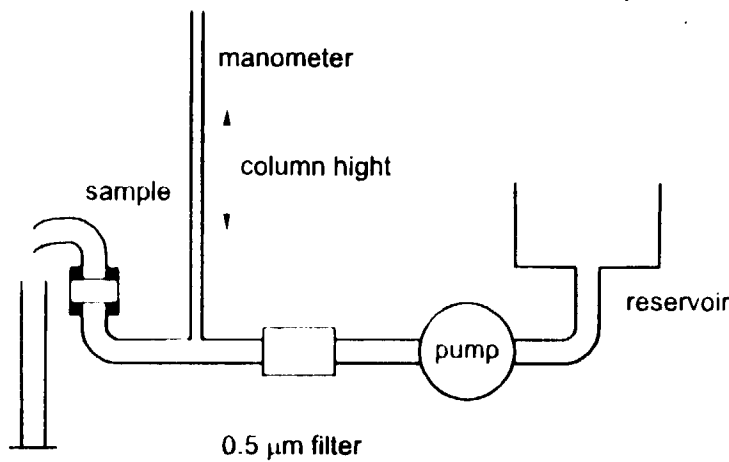
Modified fluidic testing setup for
permeability measurements.

Porous sample test section, exploded
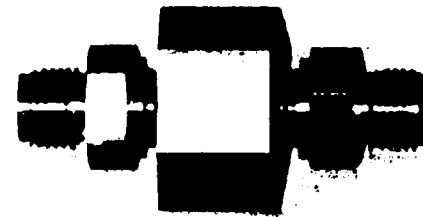
Porous sample test section, assembled

Permeability Testing

$$y = 8.8507x$$
$$R^2 = 0.9932$$

$$y = 7.9245x$$
$$R^2 = 0.9884$$

● sample 2
□ sample 3

Δp (PSI)

flow rate (ml/sec)
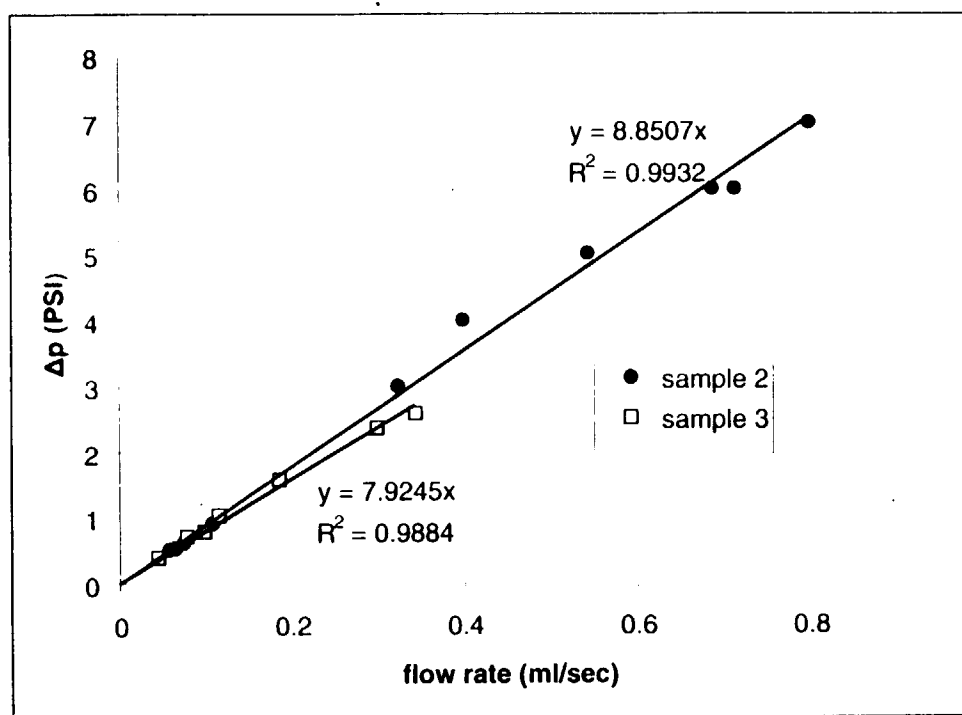
Volumetric flow rate vs. pressure drop for two samples

Theoretical Permeability Development

Pore level modeling
- Fully-Developed Laminar Flow in a Round Tube (Hagen-Poiseuillie flow):

Governing Equation

$$\frac{dP}{dx} = \mu \left(\frac{\partial^2 u}{\partial r^2} + \frac{1}{r} \frac{\partial u}{\partial r} \right) \tag{1}$$

Solution

$$U = \frac{r_o^2}{8\mu} \left(-\frac{dP}{dx} \right) \tag{2}$$

Global modeling
- Darcy model flow in the porous wick

$$u_D = \frac{K}{\mu} \left(-\frac{dP}{dx} \right) \tag{3}$$

Or

$$u_D = \frac{N\left(\pi r_o^2\right)}{A} U = \varepsilon\, U \tag{4}$$

Where

N/A	the number of pores per unit frontal area (tubes/m^2)
A	the total frontal area (m^2)
ε	the porosity

Combining (2) & (4)

$$K = \frac{\pi r_o^4}{8} \frac{N}{A} = \frac{r_o^2}{8} \varepsilon \tag{5}$$

Permeability Testing and Data Reduction

| Exp. #	ΔP [psi]	ΔP[N/m2]	ΔX [m]	$\Delta P/\Delta X$ [N/m³]	ρ[kg/m³]	μ[N.s/m²]	Q [L/s]	Q[m³/s]	A_{Pore}[m²]	U_{pore}	A_{total}	U_D [m/s]	K
1	2.45	1.69E+04	2.4E-04	-7.04E+07	1000	8.55E-04	1.38E-04	1.38E-07	3.85E-11	3.6E+03	3.2E-05	0.004365	5.30E-14
2	2.75	1.90E+04	2.4E-04	-7.90E+07	1000	8.55E-04	1.73E-04	1.73E-07	3.85E-11	4.5E+03	3.2E-05	0.005451	5.90E-14
3	3.45	2.38E+04	2.4E-04	-9.91E+07	1000	8.55E-04	2.16E-04	2.16E-07	3.85E-11	5.6E+03	3.2E-05	0.006818	5.88E-14
4	4.2	2.90E+04	2.4E-04	-1.21E+08	1000	8.55E-04	2.88E-04	2.88E-07	3.85E-11	7.5E+03	3.2E-05	0.009096	6.45E-14
5	4.9	3.38E+04	2.4E-04	-1.41E+08	1000	8.55E-04	4.87E-04	4.87E-07	3.85E-11	1.3E+04	3.2E-05	0.015357	9.33E-14
6	8.3	5.72E+04	2.4E-04	-2.38E+08	1000	8.55E-04	9.27E-04	9.27E-07	3.85E-11	2.4E+04	3.2E-05	0.029233	1.05E-13
7	1.3	8.96E+03	2.4E-04	-3.73E+07	1000	8.55E-04	5.68E-05	5.68E-08	3.85E-11	1.5E+03	3.2E-05	0.001791	4.10E-14
8	1.4	9.65E+03	2.4E-04	-4.02E+07	1000	8.55E-04	7.36E-05	7.36E-08	3.85E-11	1.9E+03	3.2E-05	0.00232	4.93E-14
9	1.65	1.14E+04	2.4E-04	-4.74E+07	1000	8.55E-04	0.000108	1.08E-07	3.85E-11	2.8E+03	3.2E-05	0.003402	6.14E-14
10	3	2.07E+04	2.4E-04	-8.62E+07	1000	8.55E-04	3.22E-04	3.22E-07	3.85E-11	8.4E+03	3.2E-05	0.010158	1.01E-13
11	4	2.76E+04	2.4E-04	-1.15E+08	1000	8.55E-04	3.97E-04	3.97E-07	3.85E-11	1.0E+04	3.2E-05	0.012527	9.32E-14
12	5	3.45E+04	2.4E-04	-1.44E+08	1000	8.55E-04	5.43E-04	5.43E-07	3.85E-11	1.4E+04	3.2E-05	0.017137	1.02E-13
13	6	4.14E+04	2.4E-04	-1.72E+08	1000	8.55E-04	6.88E-04	6.88E-07	3.85E-11	1.8E+04	3.2E-05	0.021691	1.08E-13
14	6	4.14E+04	2.4E-04	-1.72E+08	1000	8.55E-04	7.13E-04	7.13E-07	3.85E-11	1.9E+04	3.2E-05	0.022493	1.12E-13
14	7	4.83E+04	2.4E-04	-2.01E+08	1000	8.55E-04	7.98E-04	7.98E-07	3.85E-11	2.1E+04	3.2E-05	0.025157	1.07E-13
15	2	1.38E+04	2.4E-04	-5.75E+07	1000	8.55E-04	9.46E-05	9.46E-08	3.85E-11	2.5E+03	3.2E-05	0.002984	4.44E-14
16	4	2.76E+04	2.4E-04	-1.15E+08	1000	8.55E-04	3.19E-04	3.19E-07	3.85E-11	8.3E+03	3.2E-05	0.010061	7.49E-14

Average K = 7.96E-14

Permeability Testing
(Experimental Versus Theory)
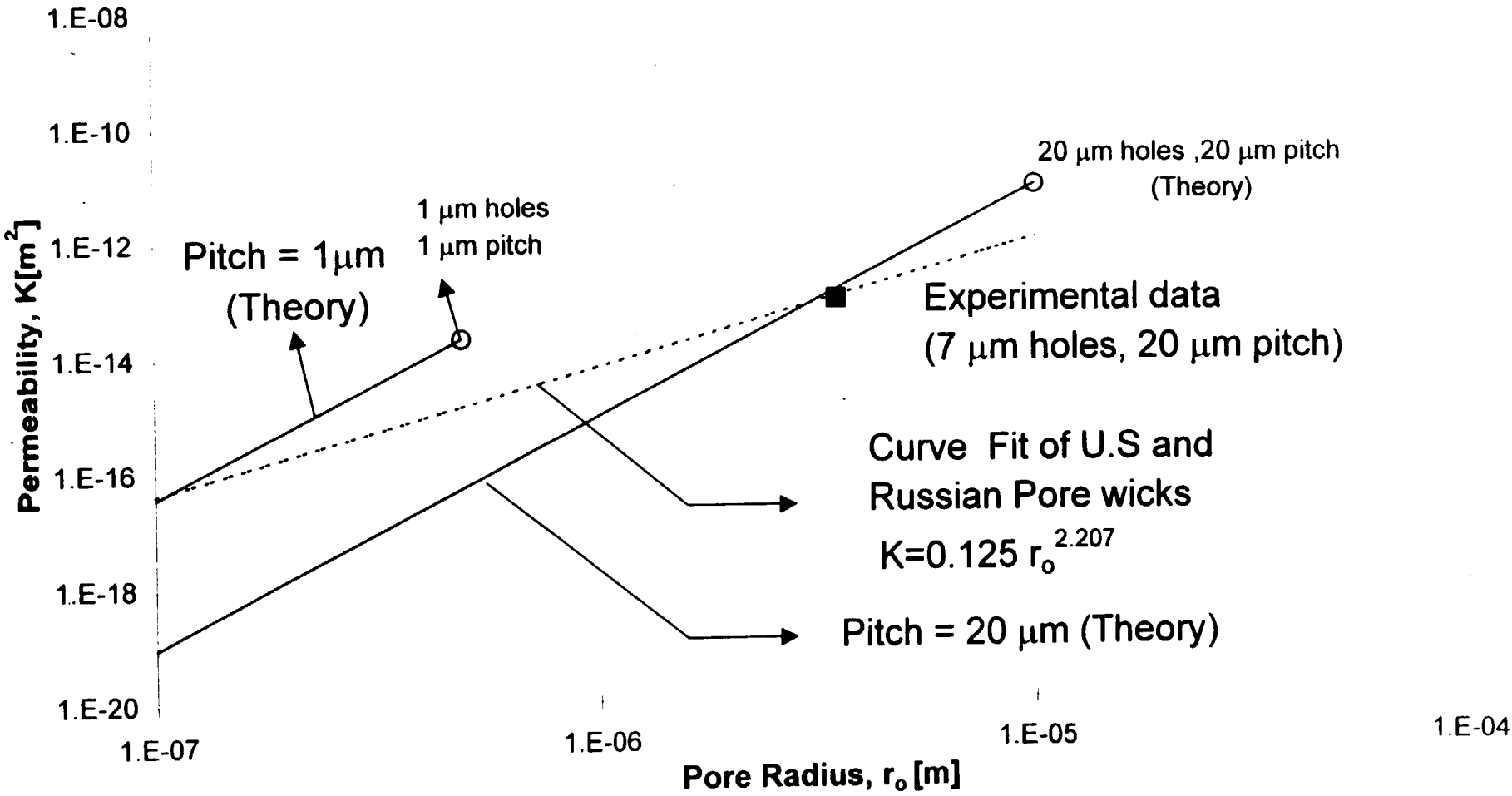
Permeability Variation with Pore Radius

Summary

- microchannels and milli-slot have been fabricated, tested and thermal model verified

- prototype MCM module with micromachined pockets and chips has been fabricated

- 3-D thermal model of MCM module is under development

- contact resistance experiments, 3-D chips-to-substrate, are almost ready to begin

- 5 μm holes x 20 μm (pitch) silicon porous wicks have been successfully fabricated

- permeability measurements of porous wick test specimens are ongoing

- 1 μm holes x 4 μm (pitch) silicon porous wicks are under fabrication

- future work

APPENDIX C

Coherent Macro Porous Silicon as a Wick Structure in an Integrated Microfluidic Two-Phase Cooling System

Alexander D. Hölke[a], Jörg Pilchowski[a], H. Thurman Henderson[a], Ahed Saleh[b], Michael Kazmierczak[b], Frank M. Gerner[b], Karl Baker[c]

[a]University of Cincinnati, Center for Microelectronic Sensors and MEMS (CMSM), P.O. Box 210030, [b]University of Cincinnati, Dept. of Mech. , Ind. and Nucl. Eng [c]NASA Lewis Research Center Cleveland, Ohio

ABSTRACT

This paper reports a new concept of building a coherent porous wick structure in planar silicon wafers for capillary pumping in Loop Heat Pipes (LHPs). By utilizing Macro Porous Silicon (MPS) fabrication technology, with pore sizes in the order of a micron, precise control of the pore dimensions of the wick is possible. In addition, by using MEMS (Micro Electro Mechanical Systems) fabrication technology, LHPs can ultimately be integrated into electronic packaging systems, or indeed into the silicon microchips themselves. The MPS samples were fabricated and tested for capillary pressure and permeability. The test results closely matched the analytical models that were derived from basic physics.

Keywords: Macro Porous Silicon (MPS), Loop Heat Pipe (LHP), wick, electronic cooling, microchannel flow

1. INTRODUCTION

Enhanced cooling of present and next generation electronic packaging systems is crucial. The realization of increased speed and higher device density result in ever-higher heat fluxes, calling for design of fully integrated packaging-cooling systems. This work reports a portion of a larger ongoing effort to develop a unique all-silicon MCM (Multi Chip Module) design [1] which includes several concurrent cooling schemes, such as forced liquid cooling in ultra deep microchannels [2], passive cooling with Loop Heat Pipes (LHPs) and more traditional air fan cooling. The passive nature of the heat pipe operation renders them particularly attractive, since no external driver is required. The porous wick in the device is itself the pump of the LHP, using only the very heat it removes.

First, this paper covers heat pipe and LHP fundamentals and the particular importance of the wick. Then, the characteristic parameters of capillary pressure and permeability are introduced and applied to the coherent wick. Macropore fabrication is included with particular attention paid to the necessary and important fabrication details. The testing results are then compared to the theoretical predictions. Finally, an integrated evaporator concept for MCMs is introduced.

2. COHERENT WICK DESIGN

Motivation

A heat pipe is a sealed device in which a working fluid circulates and constantly changes from the liquid to the gaseous phase, and vice versa (Figure 1). The evaporated liquid flows from the evaporator to the condenser end by the pressure drop created from the evaporation and condensation process. The liquid is returned to the evaporator by the capillary pressure in the wick. The input heat energy is thus converted into latent heat in the evaporator, moved in the gaseous phase to condenser, and then converted back into heat energy by the evaporation process, and the heat is then ejected at the condenser end. The evaporation and condensation process takes
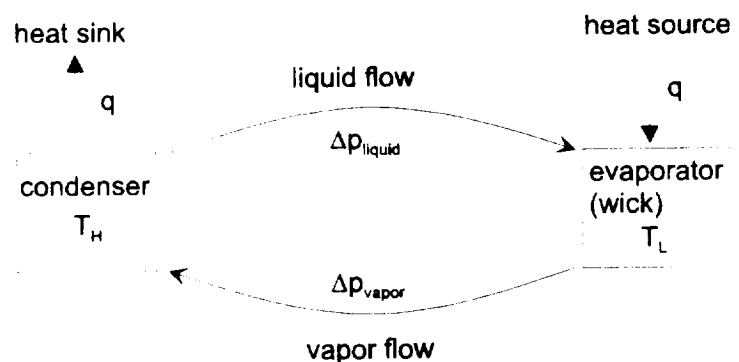

Figure 1. The basic cycle of a heat pipe.

place at almost the same temperature. i.e. it is virtually isothermal. In a 2D analogy. one often compares a heat pipe with a highly thermally conductive material. The finite heat flux q is transported at a small temperature difference ΔT. resulting in a high effective thermal conductance $G_{th,eff}$:

$$G_{th,eff} = \left|\frac{q}{\Delta T}\right|_{\Delta T \to 0} \to \infty \tag{1}$$

Heat pipes offer a passive way of rapidly transporting energy away from a heat source. The term "passive" is used here in the sense that no external action, such as pumping, is required for operation. The heat itself pumps these devices. This has certain advantages over other heat removal techniques. No extra devices (such as pumps or other actuators) are needed. and no additional power needs to be introduced as heat into the system.

The distinction between an ordinary heat pipe (HP), where a wick continuously lines the inner surface of a single pipe, and a capillary pumped loop (CPL) is that in a CPL interconnecting plumbing separates the condenser and evaporator (including the wick). The length of an ordinary heat pipe is limited, because the whole liquid return path is through the wick, which results in high viscous losses. The capillary pumped loop overcomes this shortcoming, but it is not inherently self-starting.

A recently developed type of heat pipe is the Loop Heat Pipe (LHP) [3]. It is similar in design to a Capillary Pumped Loop because it uses separate tubing for the liquid and vapor flow paths, which allows the thermal energy to be moved over relatively large distances (Figure 2). The wick is located at the evaporator and it serves as the engine, which achieves continuous circulation. The LHP is unique because the overall design provides for a reliable start-up. Working LHPs have been made using cylindrical and planar evaporator configurations.

The porous wick is without question the most important part of a LHP. It transfers the energy to the liquid-vapor interface ("meniscus") and maintains separation between the vapor and the liquid by capillary forces. The porous wick thus determines the pumping capability of a LHP like no other part. MEMS (Micro Electro Mechanical Systems) technology opens up new possibilities in wick design, as well as modeling. Traditional, sponge-like porous wicks have a randomly distributed pore size, and the flow path is irregular. Consequently, the mathematical description is statistical and semi-empirical. On the other hand, the coherent nature of wicks fabricated by the Macro Porous Silicon (MPS) etching technique allows a relatively simple analytical description of the parameters.
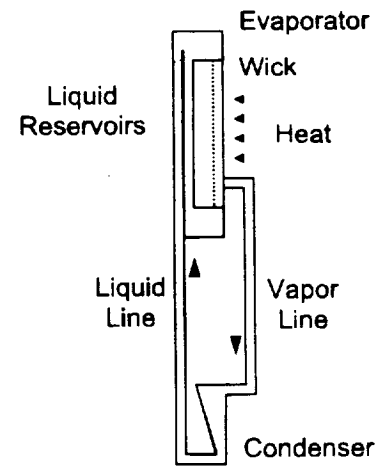

Figure 2. Schematic of a Loop Heat Pipe, redrawn from [3]

Capillary Pressure

The capillary action pumps the liquid from the condenser to the evaporator. The capillary pressure has to overcome all other pressure losses in the system. Wetting and surface tension result in a curved liquid surface, or meniscus. Macroscopically, the pressure drop ΔP_c across the meniscus is described by the surface tension σ, the wetting angle Θ, and the pore radius r_p [6]:

$$\Delta P_c = \frac{2\sigma \cos\Theta}{r_p}. \tag{2}$$

Practically, one often introduces an effective surface tension, $\sigma\cos\Theta$, since it is difficult to separate the two components in boiling experiments. In order to achieve a high capillary pressure, a small pore radius, good wetting and a liquid with large surface tension are required.

Permeability

The permeability K is a measure of the liquid flow conductance through the porous wick. It is used in the expression

$$u_{\scriptscriptstyle D} = \frac{K}{\mu}\left(-\frac{\partial P}{\partial x}\right) \qquad\qquad (3)$$

where $u_{\scriptscriptstyle D}$ is the macroscopic, volume-averaged flow velocity, μ the dynamic viscosity of the liquid, and $\partial P/\partial x$ is the axial pressure gradient. Assuming fully-developed laminar flow in the pores of the wick one can show [4] that, for an array of straight pores in a wick of porosity ε (the ratio of pore volume to total wick volume), the permeability is:

$$K = \frac{r_p^2}{8}\varepsilon . \qquad\qquad (4)$$

Thus, to maximize the liquid flow through the wick for a given pressure drop ΔP, one must choose a liquid of low viscosity, minimize the wick thickness $d_{wick}=\Delta x$, and maximize the pore radius and porosity. Note that the latter requirement contradicts that for a high capillary pressure in Eq. (2).

Fabrication

MPS technology was first developed by Lehmann [7]. It allows the formation of coherent arrays of straight pores in n-type silicon, with a pore diameter ranging from 0.2-20μm.

The fabrication process is electrochemical in nature. When properly biased, silicon etches in aqueous HF solution if electronic holes are present in the material. This is not the case for n-type silicon in the dark, thus practically no etching takes place. Under illumination electron/hole pairs are generated and n-type silicon does etch. Therefore, light is one major control mechanism for the amount of silicon etched (see Figure 3). The primary directions of pore growth are of type <100>. If the area of hole generation is limited to the backside of the wafer, the pores tend to grow toward the source of holes. The pore tips confine the electric field and consume all the holes for etching. Such a constraint of the generation region is achieved by including the IR blocking filter, limiting the light penetration depth to a small thickness on the substrate backside. On a (100) wafer, the vertical pore growth direction is one of the <100> directions. Therefore,

Figure 3. Schematic of the macropore etching setup

deep and coherent MPS can only be formed, at this point, on n-type (100) silicon wafers. Other researchers were able to form MPS on p-type wafers without illumination [8,9], but the resulting pores are not as deep and uniform as the ones described here.
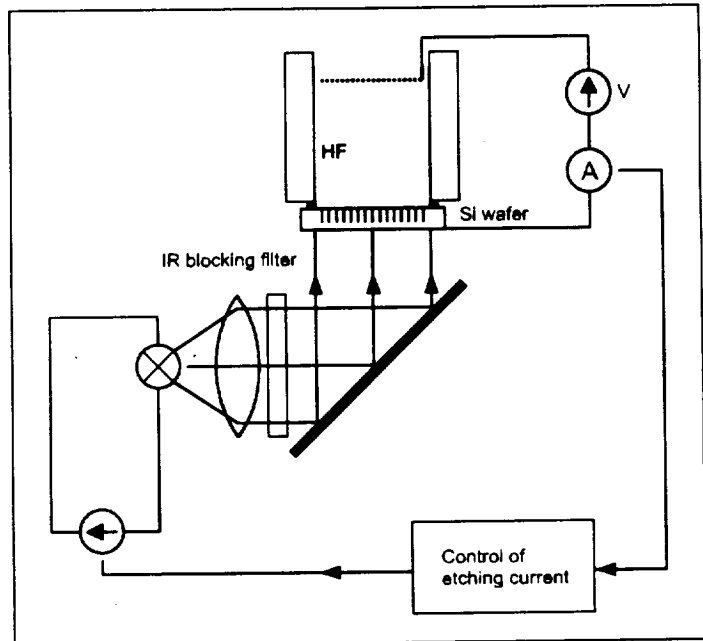
The etching at the pore tips takes place at a certain current density, J_{PS}, which is only a function of temperature and HF solution concentration (see Appendix). This means that if the latter are kept constant, the current density remains constant. Now, by changing the illumination intensity, the etching current does change. This must result in a change of the effective area that is etched, since the current density is constant. This area change translates into a change in pore diameter. Yet there is a limit of how much the pore diameter can change. The range of allowed pore sizes is determined by the substrate doping.

There is also a way to predetermine the pore pattern and thereby to achieve a very uniform pore array. Photolithography and subsequent anisotropic etching can be used to achieve a pore initiation step. The resulting pyramidal etch pits [10] are sufficient to concentrate the field at their tips and initiate pore growth at these pre-selected sites.

In summary, to achieve a desired pore pattern, one first chooses an adequate array of etch pits for pore initiation sites. This will determine the pore pitch. Then, the actual pore diameter is set roughly by the chosen doping concentration of the silicon material and "fine-tuned" by the amount of illumination. Since the etching current can be easily measured, the diameter can

be accurately controlled. Small changes in pore diameter are possible within the range allowed by the doping constraint. Finally, the pore tip etches with an etch rate that is proportional to the current density J_{ps}. Thus, the desired pore depth is achieved by timing the etching process.

The etching, however, cannot quite continue through the whole wafer thickness because of two reasons: (1) The pores at some point cannot grow towards the source of holes as they etch into the generation region, because the field confinement of the pore tips is not effective any longer. Thus, as the pores approach the broad backside field plane, they tend to branch. (2) The HF would leak out of the setup and damage the optics in our system. Instead of etching pores through the entire wafer thickness, the pores are etched through most of the wafer, and then, the wafer is selectively etched from the backside using TMAH or another appropriate etchant, until the pore region is reached.

Lehmann [7] already pointed out that the etching process leads to an effective decrease in HF solution concentration at the pore tips, resulting in a parabolic development of the pore depth over time. It was found in the present study that this also leads to an increase in pore diameter with increasing depth if the etching current is kept constant (Figure 4). Based on the parabolic development of the pore depth, the concentration change can be calculated and the current can be appropriately adjusted (see Appendix). Samples etched with these improved parameters exhibit a constant pore cross-section (Figure 5).
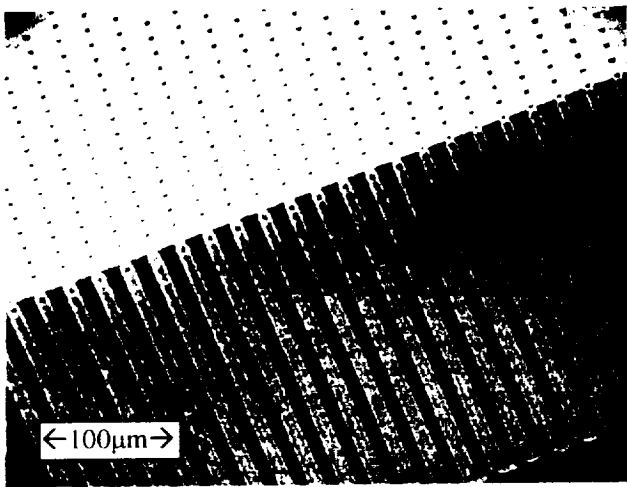

Figure 4. Cross-sectional view of a sample etched at a constant current. The diameter increases with depth.
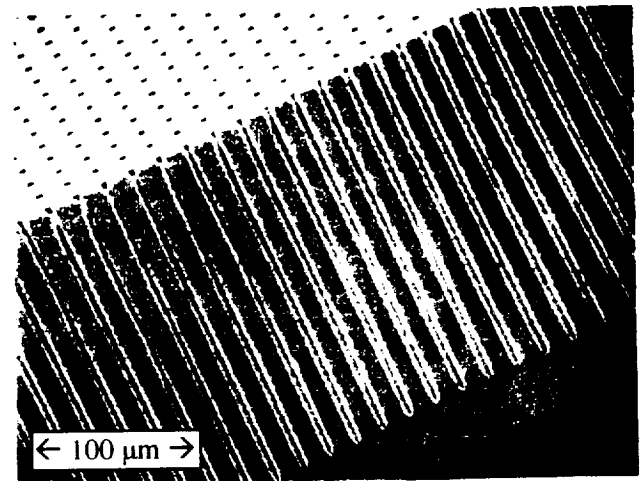
Figure 5. A sample etched with a current that was adjusted to yield a constant pore cross-section (appendix).

Thus far, wicks with pores of about 5-7μm pore diameter and a pitch (center-to-center distance) of 20μm were fabricated. At the moment, our effort is centered towards fabrication of pores with a smaller diameter (1μm) and a smaller pitch (4μm).

Testing setup for Measurement of Permeability and Capillary Pressure

Deionized water was used for the flow tests, where the pressure drop across the porous sample was measured using a manometer, and the flow rate was determined by collecting the volume of liquid over a certain time duration (Figure 6).

The capillary pressure was obtained using the same setup. Initially, with only liquid on the pump side and air on the other side of the porous wick sample, menisci formed at the interface. The liquid initially did not flow, and pressure builds up. Only when the pressure exceeds the capillary pressure does the liquid begin to flow, and the pressure drop across the sample decreases suddenly. The pressure falls to the value determined by the permeability of the sample. The maximum pressure obtained before the flow starts is the capillary pressure.
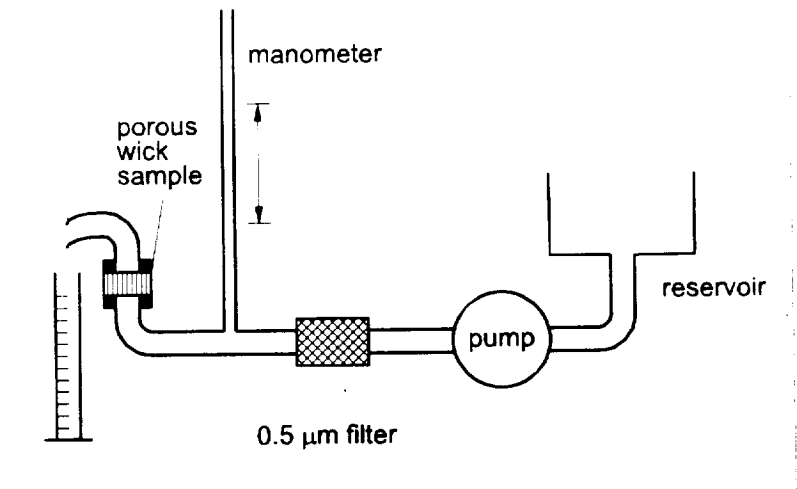
Figure 6. Testing setup for capillary pressure and permeability.

3. RESULTS

As Eq. (3) suggests, the permeability of the sample can be deducted from the slope in the flow / pressure drop diagram. For one test run, a line was fitted into the data field (Figure 7) and the permeability calculated. The results of the tests along with the theoretical predictions, as well as test data from conventional sintered porous metal wicks [4], are plotted in Figure 8. Although permeability data were collected from samples of only one wafer, the results so far confirm the theoretical predictions. Even with its low porosity (7%), in terms of permeability the coherent MPS wick performs as well as the conventional porous metal wicks (themselves a fairly recent development) which frequently have a porosity value in excess of 50%.

The capillary pressure tests conducted to date are not very precise since the tests were primarily conducted to collect flow data for permeability measurements (TABLE 1). The additional data shown in the table are measurements taken by Thermacore [11] (commercial developer of porous metal wicks) with the so-called bubble-point test. Their results also show a rather high degree of uncertainty. However, the theoretically predicted radii derived from the measured capillary pressure are also close the SEM measurements.
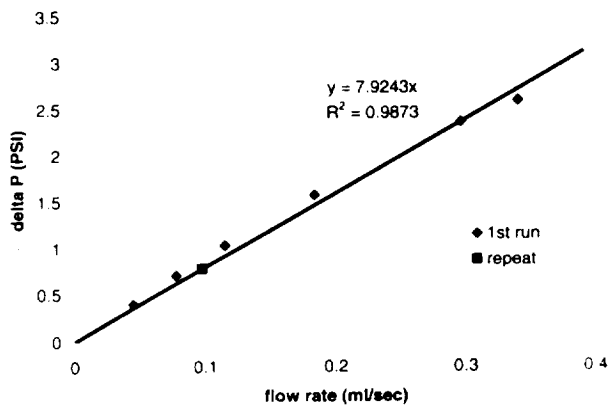
Figure 7. Example of a flow rate versus pressure drop test. The slope is inversely proportional to the permeability.
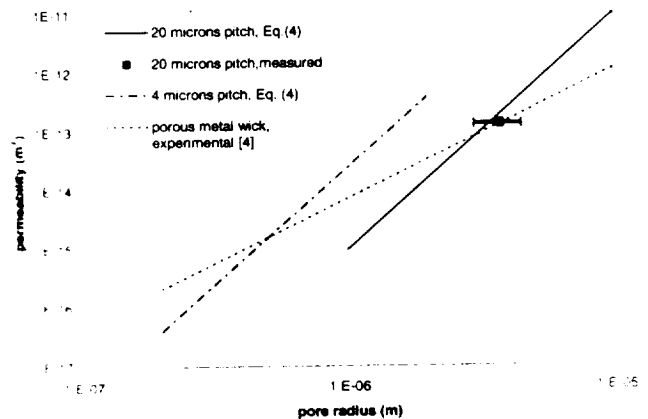
Figure 8. Permeability vs. pore radius for two different pore initiation patterns (masks), as well as conventional porous metal wicks. The theoretical and test results match well.

TABLE 1.
Capillary pressure test results

Test Lab	Wafer	r_{min} (μm) (from SEM)	fluid	Test #	Δp (psi)	r_{min} (μm) (from Δp)
Univ. of Cincinnati	PS20	3.25	water		6 - 8	2.6 - 3.5
Thermacore [11]	PS17	2.5	acetone	5	1.17	2.825
				6	1.27	2.6
				7	1.55	2.225
				8	1.41	2.44

4. INTEGRATION

The coherent MPS wick must be ultimately integrated into a working LHP. This would be necessary to clearly demonstrate the feasibility of using a MPS wick.

Anisotropic etching and wafer bonding techniques can be used to create a flat evaporator (Figure 9). On the vapor side, energy is conducted to the wick by an array of mesas from the hot plate. This plate is anisotropically etched from a (100) silicon wafer using KOH and appropriate corner compensation techniques. The volume between the mesas provides the vapor flow path. This hot plate could be attached directly to an MCM, or be itself part of the all-silicon MCM [1]. The porous silicon plate and the bottom plate form part of the liquid reservoir.
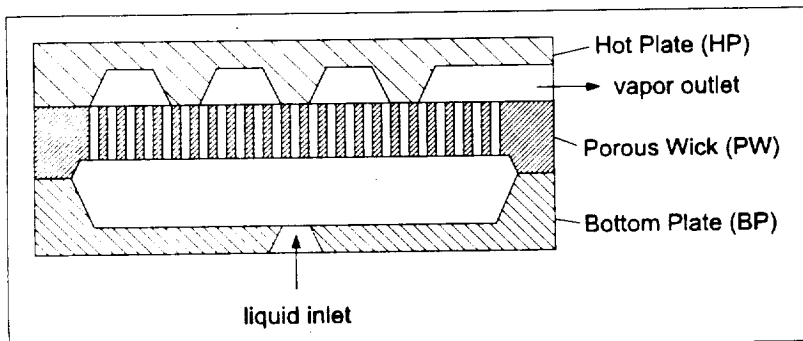

Figure 9. Cross-sectional view of an evaporator fabricated by MEMS technology.

This integrated planar evaporator will replace the conventional, cylindrical evaporator of a working LHP. It is extremely important that the evaporator is flat for MCM cooling applications, and so far conventional porous metal wicks could not achieve this goal because only cylindrical evaporator sections have been made. Ultimately, in the future it is envisioned that a whole LHP is fabricated by MEMS (Micro Electro Mechanical Systems) technology.

5. CONCLUSIONS

MPS was used to create a new type of wick for use in LHPs. The good dimensional control of pore size and pattern offered via state-of-the-art MEMS-based micromachining allows optimal fine-tuning of the wick's parameters, such as permeability and capillary pressure. The feasibility of fabricating a novel wick by MPS etching was demonstrated. Relative simple analytical modeling of important performance parameters of the wick was carried out and was verified experimentally.
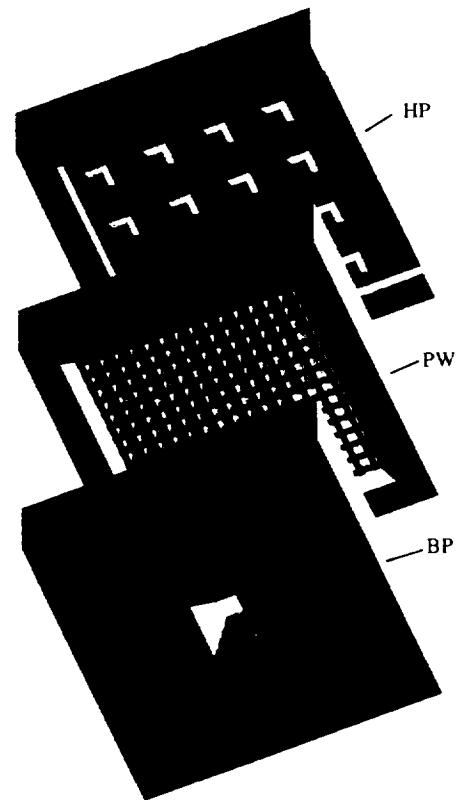

Figure 10 Exploded view of the integrated evaporator

Operation of the micromachined silicon wick in an actual LHP has yet to be confirmed. A parametric study is also suggested to optimize the wick performance, as well as the thermal and mechanical integration with a LHP.

In terms of permeability and capillary pressure, the porous silicon wick is at least as good as are conventional porous metal wicks, even at a far lower porosity. Being a MEMS-type component, the porous silicon wick has several advantages. It is inherently planar, can be made very thin, and it can be integrated directly and intimately with other MEMS components.

6. ACKNOWLEDGMENTS

7. REFERENCES

1. J. Pilchowski, A. Hölke, H.T. Henderson, T. M. Harms, M. Kazmierczak, F. M. Gerner, K. Baker, "All Silicon Multi Chip Module With a Fully Integrated Cooling System", *International Conference and Exhibition on Multichip Modules and High Density Packaging, Denver*, CO, 1998

2. T. M. Harms, M. Kazmierczak, F. Gerner, A. Hölke, J. Pilchowski, H. T. Henderson, K. Baker, "Experimental Investigation of Heat Transfer and Pressure Drop Through Deep Microchannels in a (110) Silicon Substrate", *Proceedings of the 1997 International Mechanical Engineering Congress and Exposition, Dallas, TX*, 1997

3. D. M. Ernst, A. L. (F.) Phillips, I. S. Rozin, "Loop Heat Pipes – Their Potential", *AIP conference proceedings*, pp. 953-964, 1994

4. N. Gernert, G. Baldassarre, J. Gottschlich, "Fine Pore Loop Heat Pipe Wick Structure Development", *Proceedings of Aerospace Atlantic Conference*, SAE paper #961319, pp. 1-10, 1996

5. A. Bejan, "Convection Heat Transfer", John Wiley & Sons, 2nd Edition, p. 570 (problem 12.2.), 1995

6. C. Arora, "Physics", S. Chand & Company Ltd., New Delhi, pp. 156-160, 1980

7. V. Lehmann, "The Physics of Macropore Formation in Low Doped n-Type Silicon", *J. Electrochem. Soc.*, Vol. 140, No. 10, pp. 2836-2843, 1993

8. E. A. Ponomarev, C. Lévy-Clément, "Macropore Formation of p-Type Si in Fluoride Containing Organic Electrolytes", *Electrochem. and Solid-State Letters*, Vol. 1, pp 42-45, 1998

9. E. K. Probst, P. A. Kohl, "The Electrochemical Oxidation of Silicon and Formation of Porous Silicon in Acetonitrile", *J. Electrochem. Soc.*, Vol. 141, pp 1006-1013, 1994

10. K. E. Bean, "Anisotropic Etching of Silicon", *IEEE Transactions of Electron Devices*, Vol. ED-25, pp 1185-1193 ,1978

11. A. L. (F) Phillips, private communications, 1998

8. APPENDIX

A: coefficient
c: HF solution concentration in wt.%
c_0: initial HF solution concentration
C: pre-exponential factor (3300 A/cm^2 wt.%$^{2/3}$)
d: pore cross-sectional diameter
e: elementary charge
E_a: activation energy (0.345eV)
I: etching current
J_{PS}: critical current density
$J_{PS,0}$: initial critical current density
k: Boltzmann constant
L: pore length (depth)
n: dissolution valence (2.4)
N_{Si}: atomic density of silicon

t: time
T: temperature in K
v: pore growth velocity (etch rate)
v_0:   initial pore growth velocity

Lehmann [7] determined the Arrhenius-type critical current density (at which the silicon is etched at the pore tips):

$$J_{PS} = Cc^{3/2} \exp\left(\frac{-E_a}{kT}\right),$$ (5)

and the etching velocity, or etch rate

$$v = \frac{J_{PS}}{n \cdot (-e) \cdot N_{Si}}.$$ (6)

Lehmann also experimentally determined the following description of the pore depth with time, for a 2.5 wt.% HF solution at room temperature:

$$\frac{t}{\text{min}} = \frac{1.89}{\mu m}L + \frac{0.0029}{\mu m^2}L^2.$$ (7)

Using Eqs. (5) and (6), one obtains the following relation for the decrease in HF concentration at the pore tips:

$$\frac{c}{c_0} = \sqrt[3]{\frac{1}{1+\dfrac{t}{308\,\text{min}}}}$$ (8)

This reduction is significantly different from the linear fit of Lehmann, for an etching time more than about 6 hours or 150μm deep (Figure 11)! Now, Eq. (5) yields the relation for correcting the current:

$$\frac{I_{etching}}{I_{etching,0}} = \frac{J_{PS}}{J_{PS,0}} = \left(\frac{c}{c_0}\right)^{3/2} = \sqrt{\frac{1}{1+\dfrac{t}{308\,\text{min}}}}.$$ (9)

Also the pore widening such as in Figure 4 (when etching without this current correction) can be predicted (Figure 12):

$$\frac{d}{d_0} = \left(\frac{c_0}{c}\right)^{3/4} = \sqrt{1+\frac{L}{326\mu m}}.$$ (10)

For different HF concentrations and temperatures a relationship similar to Eq. (7) has to be found. The general form is

$$t = v_0^{-1}L + A(c,T)L^2$$

Thus, a single test is sufficient to determine the coefficient A, and it can be decided if a current correction is necessary.
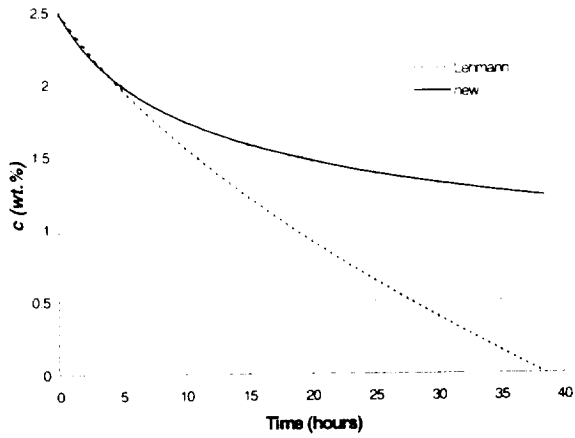
Figure 11   Decrease in HF concentration after Lehmann and with the present newly refined model.
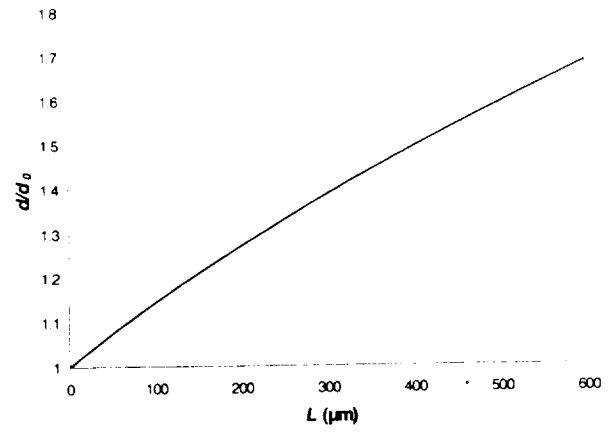

Figure 12. Calculated relative increase in pore diameter when etching with a constant current.